Article

Effects of Microstructure on Electrode Properties of Nanosheet-Derived $H_x(Ni_{1/3}Co_{1/3}Mn_{1/3})O_2$ for Electrochemical Capacitors

Masato Yano [1,*], Shinya Suzuki [1], Masaru Miyayama [1,2] and Masataka Ohgaki [3]

[1] Research Center for Advanced Science and Technology, The University of Tokyo, 4-6-1 Komaba, Meguro-ku, Tokyo 153-8904, Japan; E-Mails: sin@crm.rcast.u-tokyo.ac.jp (S.S.); miyayama@rcast.u-tokyo.ac.jp (M.M.)

[2] Japan Science and Technology Agency, CREST, 5 Sanbancho, Chiyoda-ku, Tokyo 102-0075, Japan

[3] Yokohama Laboratory, Hitachi High-Tech Science Corporation, 1-18-2 Hakusan, Midori-ku, Yokohama, Kanagawa 226-0006, Japan; E-Mail: ogaki-masataka@hhs.hitachi-hitec.com

* Author to whom correspondence should be addressed; E-Mail: masatoyano@crm.rcast.u-tokyo.ac.jp; Tel.: +81-3-5452-5082; Fax: +81-3-5452-5083.

Abstract: Nanosheet-derived $H_x(Ni_{1/3}Co_{1/3}Mn_{1/3})O_2$ was prepared by restacking $(Ni_{1/3}Co_{1/3}Mn_{1/3})O_2$ nanosheets with large or small lateral sizes and their electrochemical properties in a 1 M KOH aqueous solution; microstructural factors were compared with those of bulk $H_x(Ni_{1/3}Co_{1/3}Mn_{1/3})O_2$ (HNCM). The electrodes composed of small nanosheets exhibited very large capacitances of 1241 $F \cdot g^{-1}$ (395 $mAh \cdot g^{-1}$) at a current density of 50 $mA \cdot g^{-1}$, and 430 $F \cdot g^{-1}$ (100 $mAh \cdot g^{-1}$) at a large current density of 1000 $mA \cdot g^{-1}$. These large capacitances resulted from a heterogeneous layer structure with a large surface area and pore volume. The electrodes of large nanosheets, with a strongly interconnected microstructure and a surface area slightly larger than that of HNCM, exhibited good cycle stability and capacitances larger than that of HNCM. Microstructural control through the restacking of $(Ni_{1/3}Co_{1/3}Mn_{1/3})O_2$ nanosheets improved the electrochemical properties of $H_x(Ni, Co, Mn)O_2$.

Keywords: nanosheets; $H_x(Ni; Co; Mn)O_2$; layer-structured materials; electrochemical capacitors; energy storage devices

1. Introduction

The demand for energy storage devices with high power density, high energy density, and high safety, especially for use in power tools and electric hybrid vehicles, is increasing. Electrochemical capacitors have attracted considerable attention as one such type of device because of their high power density, long cycle life, and relatively high energy density [1–3]. Moreover, these capacitors are expected to have a high level of safety, especially those that use aqueous solution electrolytes instead of organic electrolytes.

In electrochemical capacitors, electric energy is stored by means of a pseudocapacitive process based on Faradaic redox reactions near the surface of active materials, as well as a capacitive process through charge separation at the electrode/solution interface. Ruthenium oxide has been studied as a cathode material for electrochemical capacitors because of its high electronic conductivity and large capacitance of up to 1580 $F \cdot g^{-1}$ (in very thin films) [4–8]. However, ruthenium oxide is not naturally abundant, and various metal oxides such as V_2O_5, MoO_3, and MnO_2 have been studied as alternate electrode materials [9–22]. Manganese and vanadium oxides are expected to have large capacitances because their cations take several oxidation states within the potential window of an aqueous solution. In the case of manganese oxides, it is advantageous to use strong basic solutions in which MnO_2 and $Mn(OH)_2$ can exist in solid form [23,24]. However, most Mn-containing compounds exhibit poor cyclic stabilities in basic solutions because of an irreversible phase transformation into spinel-type Mn_3O_4 [20,22,25].

Layer-structured $Li(Ni_{1/3}Co_{1/3}Mn_{1/3})O_2$ is a promising cathode material for Li–ion batteries [26–34]. Excellent electrochemical properties have been reported for this material, such as large capacities of approximately 150–190 $mAh \cdot g^{-1}$ (284–360 $F \cdot g^{-1}$, 2.5–4.4 V *vs.* Li/Li$^+$) with high cycle stabilities and improved electric conductivities achieved through Co-doping [26,27]. We focused on (Ni, Co, Mn) oxides as electrode materials for electrical capacitors, and reported that protonated $H_x(Ni_{1/3}Co_{1/3}Mn_{1/3})O_2$ (HNCM) has a large capacitance of 400–720 $F \cdot g^{-1}$, high rate capability, and good cycle stability even in a basic KOH aqueous solution [35]. The large capacitance was confirmed to be due to Faradaic redox reactions of component metal ions.

Nanosheets are obtained by delaminating layered materials such as layer-structured compounds into one or more layers [36–41]. The thickness of nanosheets is on the nanometer scale, and their lateral dimensions are on the submicrometer to micrometer scale. They are obtained in a colloidal suspension, and their restacking results in a specific surface area much larger than that of conventional particles/powders [6,19,20,36,37]. It has been reported that nanosheet-derived materials exhibit excellent properties as cathode materials for Li–ion batteries [36,37] and electrochemical capacitors [6,19,20]. Because of its low ion diffusion resistance, nanosheet-restacked MnO_2 exhibits a larger capacitance (173 $F \cdot g^{-1}$) than bulk materials do at high current densities [19].

In the present study, we attempted to improve the electrode properties of layer-structured HNCM by controlling the electrode microstructure through the restacking of $(Ni_{1/3}Co_{1/3}Mn_{1/3})O_2$ nanosheets. $(Ni_{1/3}Co_{1/3}Mn_{1/3})O_2$ nanosheets were obtained by the exfoliation of HNCM. Nanosheet-restacked materials were obtained by restacking the $(Ni_{1/3}Co_{1/3}Mn_{1/3})O_2$ nanosheets with different lateral sizes by using an HCl aqueous solution. HNCM and nanosheet-restacked materials were evaluated by various

methods in order to investigate their electrochemical properties and the effects of microstructural changes on the electrode properties.

2. Results and Discussion

2.1. Microstructures

2.1.1. AFM Observation of Nanosheets

$(Ni_{1/3}Co_{1/3}Mn_{1/3})O_2$ nanosheets were obtained by the exfoliation of layer-structured HNCM [41]. Layer-structured $Li(Ni_{1/3}Co_{1/3}Mn_{1/3})O_2$ (LNCM) was synthesized via a co-precipitation method [28]. A colloidal suspension of $(Ni_{1/3}Co_{1/3}Mn_{1/3})O_2$ nanosheets with small and large lateral sizes (small- and large-NS, respectively) were obtained by multistep centrifugation at different rotation speeds as reported previously [21].

Nanosheet sizes were confirmed by atomic force microscopy (AFM) observations. Figure 1 shows the AFM images of the obtained nanosheets deposited on a mica substrate. Large- and small-NS had widths of 50–600 and 50–100 nm, respectively, and thicknesses of 2–3 and 1–2 nm, respectively.

Figure 1. AFM images of (**a**) large-NS and (**b**) small-NS.
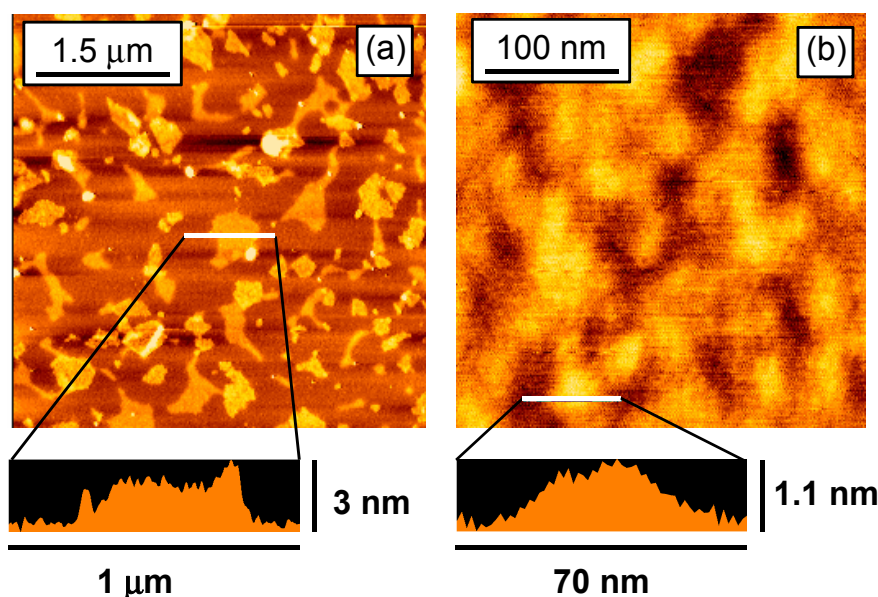

2.1.2. XRD Measurements of Nanosheet-Restacked Materials

Small-NS-restacked materials (as-prepared S-NS-NCM) and large-NS-restacked materials (L-NS-NCM) were obtained by reacting the $(Ni_{1/3}Co_{1/3}Mn_{1/3})O_2$ nanosheet colloidal suspensions with a 1 M HCl aqueous solution. S-NS-NCM was obtained by ball milling of as-prepared S-NS-NCM to reduce its particle size.

The crystal structures of the particles were confirmed by performing X-ray diffraction (XRD) analysis. Figure 2 shows the XRD patterns for HNCM, L-NS-NCM, as-prepared S-NS-NCM, and S-NS-NCM. The XRD pattern for HNCM exhibited sharp diffraction peaks corresponding to a layered structure similar to that of LNCM. This indicates that HNCM had a regularly stacked layer structure

similar to that of LNCM. On the other hand, the XRD pattern for L-NS-NCM and as-prepared S-NS-NCM exhibited broad diffraction peaks. Furthermore, in the case of S-NS-NCM, the diffraction peaks corresponding to the layered structure were quite weak. These results suggest that nanosheet-restacked materials, especially S-NS-NCM, had irregularly stacked layered microstructures.

Figure 2. XRD patterns for (**a**) HNCM; (**b**) L-NS-NCM; (**c**) as-prepared S-NS-NCM; and (**d**) S-NS-NCM.
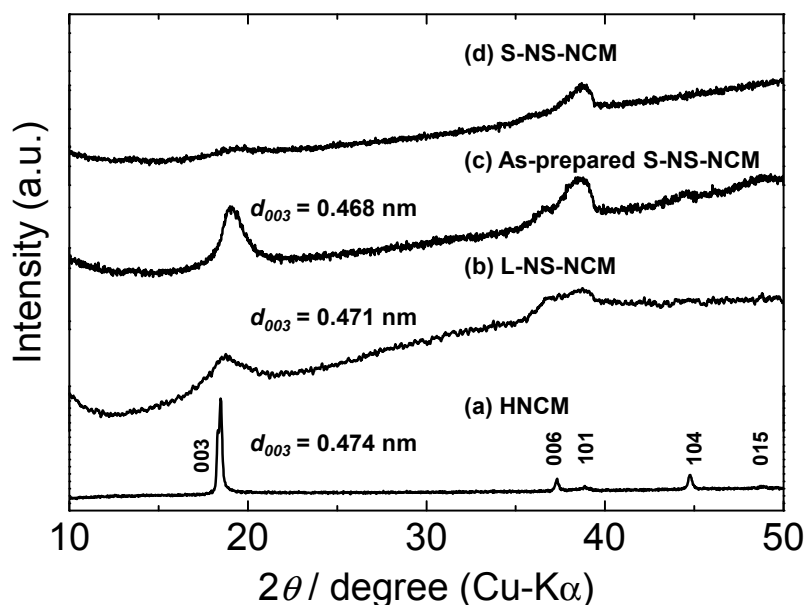
2.1.3. SEM Observation of Nanosheet-Restacked Materials

The morphologies of the particles were observed by scanning electron microscopy (SEM). Figure 3 shows the SEM images of HNCM, L-NS-NCM, as-prepared S-NS-NCM, and S-NS-NCM. HNCM was made up of polygonal particles with sizes ranging from 500 nm to 2 μm. L-NS-NCM contained large particles of approximately 1–20 μm in size, and large-NS stacked on the surface of these particles. As-prepared S-NS-NCM contained large particles approximately 3–50 μm in size, which were composed of irregularly agglomerated small nanosheets of the size 50–100 nm. The particle size of ball-milled S-NS-NCM was reduced to 300 nm to 3 μm, which was almost equal to that of HNCM.

The cross-sections of L- and S-NS-NCM particles were also observed by SEM. The cross-sections were prepared by the focused ion beam method. Figure 4 shows the cross-sectional SEM images of L- and S-NS-NCM. Both S- and L-NS-NCM contained numerous pores. In the case of L-NS-NCM, curved large-NS layers were stacked over each other and were strongly interconnected. Moreover, L-NS-NCM maintained a layered structure in the stacked parts. On the other hand, S-NS-NCM had an irregularly stacked layered microstructure made up of small-NS. The interconnection between small-NS layers in S-NS-NCM seemed relatively weaker than that between large-NS layers in L-NS-NCM.

Figure 3. SEM images of (**a**) HNCM; (**b**) L-NS-NCM; (**c**) as-prepared S-NS-NCM; and (**d**) S-NS-NCM.
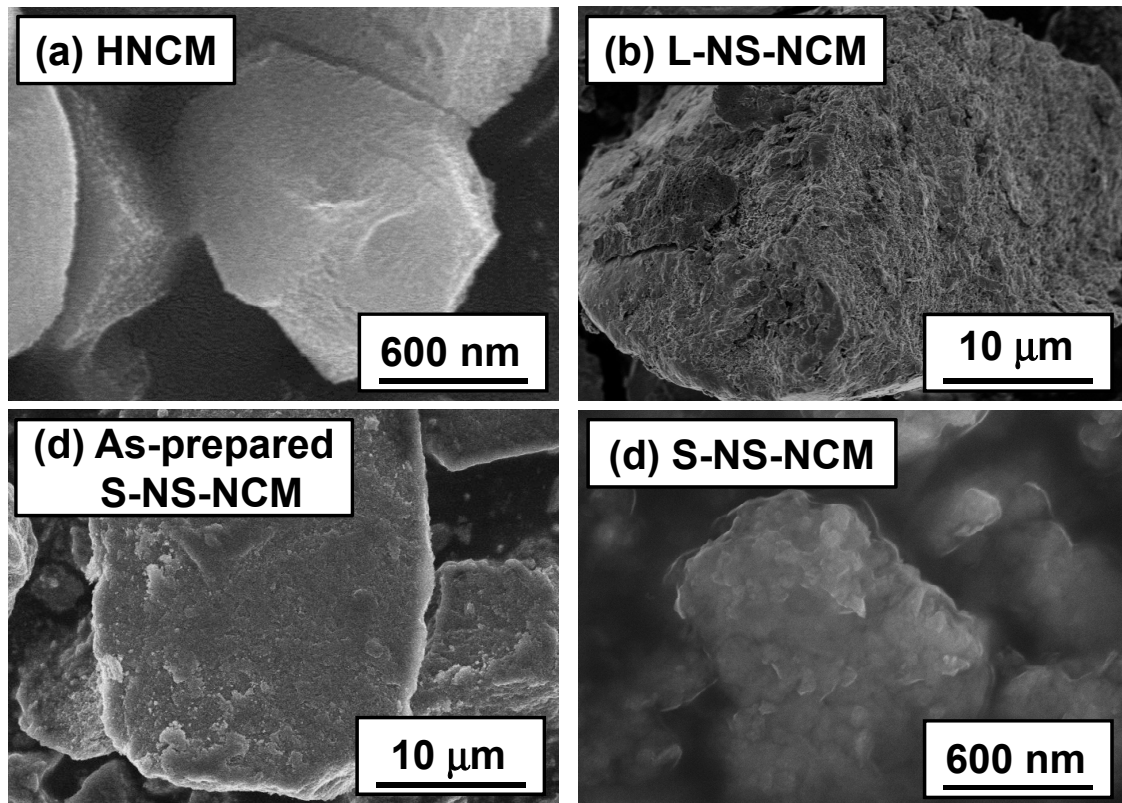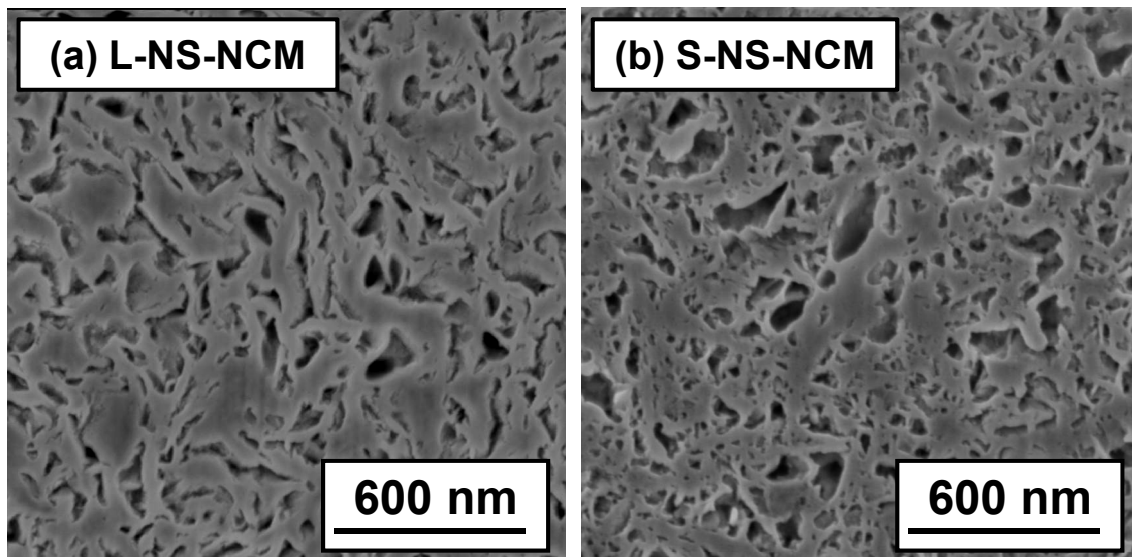

Figure 4. Cross-sectional SEM images of (**a**) L-NS-NCM and (**b**) S-NS-NCM.

2.1.4. BET Analysis

Table 1 lists the particle size, specific surface area, and pore volume of HNCM, L-NS-NCM, as-prepared S-NS-NCM, and S-NS-NCM. L-NS-NCM had a specific surface area and pore volume of 8 $m^2 \cdot g^{-1}$ and 0.02 $cm^3 \cdot g^{-1}$, respectively. These values were almost equal to those for HNCM. On the other hand, as-prepared S-NS-NCM and S-NS-NCM had large specific surface areas of 80 and

56 $m^2 \cdot g^{-1}$, respectively, and large pore volumes of 0.22 and 0.14 $cm^3 \cdot g^{-1}$, respectively. The surface areas and pore volumes were increased considerably when small-NS was used.

Table 1. Particle size, specific surface area, and pore volume of HNCM, L-NS-NCM, as-prepared S-NS-NCM, and S-NS-NCM.

Electrodes	Particle size (µm)	Specific surface area (m^2 g^{-1})	Pore volume ($cm^3 \cdot g^{-1}$)
HNCM	0.5–2	6	0.02
L-NS-NCM	1–20	8	0.02
As-prepared S-NS-NCM	3–50	80	0.22
S-NS-NCM	0.5–3	56	0.14

2.1.5. Summary of Microstructures

The difference in the microstructures of the various samples can be clearly observed from the results of XRD analysis, SEM observations, and BET analysis. HNCM had a homogeneous layered microstructure, while S-NS-NCM had an irregularly stacked layered microstructure. L-NS-NCM had an intermediate structure. L-NS-NCM had a small surface area and pore volume comparable to the surface area and pore volume of HNCM, probably because of its large particle size and surface covered with large-NS. On the other hand, S-NS-NCM had a heterogeneous microstructure with a large surface area and pore volume due to the heterogeneous layered microstructure consisting of small-NS.

2.2. Electrochemical Properties

The electrochemical properties of HNCM and NS-NCM were investigated using cyclic voltammetry (CV) tests, constant current charge/discharge tests, and AC impedance measurements. The general reaction mechanisms are first discussed, followed by the experimental results for the electrodes.

2.2.1. General Charge Storage Mechanisms

In electrochemical capacitors, charge is stored via both non-Faradaic capacitive processes and Faradaic pseudocapacitive processes. In a non-Faradaic process, charge is stored rapidly by an electric double layer at the surface of the electrode, which usually has a small charge density of 16–50 $\mu C \cdot cm^{-2}$. In the case of a Faradaic process for metal dioxide (MeO_2) electrodes, two mechanisms were proposed by Toupin *et al.* [13].

The first is the adsorption of an alkali metal cation (C^+) such as K^+, Na^+, or Li^+ in the electrolyte on the surface of the active material.

$$(MeO_2)_{surface} + C^+ + e^- \leftrightarrow (MeO_2^- C^+)_{surface} \tag{1}$$
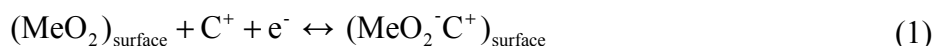
The second is the insertion of protons (H^+) or alkali metal cations (C^+) such as K^+, Na^+, or Li^+ into the lattice of the materials.

$$MeO_2 + H^+ + e^- \leftrightarrow MeOOH \tag{2}$$

or

$$MeO_2 + C^+ + e^- \leftrightarrow MeOOC \tag{3}$$
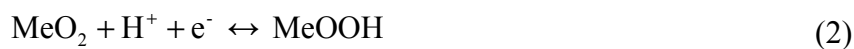
Both the aforementioned mechanisms are based on a redox reaction between Me^{3+} and Me^{4+}. For an alkaline solution system, the following two-step process has been proposed for proton insertion into MeO_2 [42–44]. In the first step, an electron from the external circuit is inserted into MeO_2 to reduce Me^{4+} to Me^{3+}. In the next step, in order to maintain the charge balance, a water molecule present at the MeO_2/electrolyte interface is decomposed into a proton, which is inserted into the lattice of MeO_2, and an OH^- ion, which diffuses from the interface into the electrolyte.

$$MeO_2 + H_2O + e^- \leftrightarrow MeOOH + OH^- \tag{4}$$

Me^{3+} is reduced to Me^{2+} in the same way.

2.2.2. Cyclic Voltammograms

Figure 5 shows cyclic voltammograms (CVs) of HNCM and S-NS-NCM in a 1 M KOH aqueous solution recorded at a sweep rate of 0.1 mV·s^{-1}. The redox peaks were observed at almost equal potentials for both HNCM and S-NS-NCM, although S-NS-NCM exhibited larger and broader redox current peaks than HNCM did. This suggests a decrease in the reaction resistance of S-NS-NCM. As reported in our previous study, in which XANES analysis was used for bulk HNCM [35], the reaction of HNCM in an alkaline aqueous system is considered to be a redox reaction between $H_{2/3}(Ni^{4+}_{1/3}Co^{3+}_{1/3}Mn^{4+}_{1/3})O_2$ and $(Ni^{2+}_{1/3}Co^{2+}_{1/3}Mn^{2+}_{1/3})(OH)_2$ via reversible insertion/extraction of H^+. On the basis of the reported redox potential of each ion, the redox currents can be assigned to Ni^{4+}/Ni^{2+}, Co^{3+}/Co^{2+}, and Mn^{4+}/Mn^{2+} redox reactions [25,45,46], as shown in Figure 5. The reduction current for Co^{3+} to Co^{2+} was not clearly observed. The reason for this can be that Co^{3+}/Co^{2+} and Mn^{4+}/Mn^{2+} reductions occurred simultaneously at the Mn^{4+}/Mn^{2+} reduction potential, as reported in the previous study [35]. Only Ni^{4+}/Ni^{2+} and Co^{4+}/Co^{3+} redox reactions have been reported in previous investigations of the Li insertion/extraction reactions occurring in LNCM in organic electrolyte systems [29–31], and Co^{3+}/Co^{2+} and Mn^{4+}/Mn^{2+} redox reactions observed in the CVs here have never been reported. Co^{3+}/Co^{2+} and Mn^{4+}/Mn^{2+} redox reactions are thus unique to HNCM in an aqueous solution.

**Figure 5.** Cyclic voltammograms of HNCM and S-NS-NCM at a sweep rate of 0.1 mV·s^{-1}. The potential range was −0.85–0.55 V *vs.* Hg/HgO.
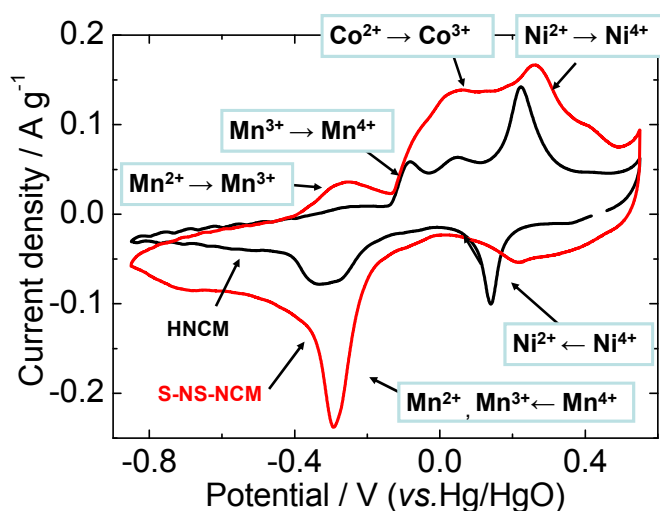
2.2.3. Charge/Discharge Curves

Figure 6 shows the charge and discharge curves for HNCM, L-NS-NCM, and S-NS-NCM at a current density of 300 mA·g^{-1}. In the second cycle, L-NS-NCM and S-NS-NCM showed enhanced capacitances. Two plateaus were observed in the discharge curves. The higher plateau seemed to correspond to the redox reaction of Ni^{4+}/Ni^{2+}, and the lower plateau seemed to correspond to the reactions of Mn^{4+}/Mn^{2+} and Co^{3+}/Co^{2+}. The differences between the plateau potentials of the charge and discharge curves decreased for L- and S-NS-NCM, which suggested a decrease in the reaction resistance of the nanosheet-derived electrodes.

Figure 6. Charge/discharge curves for HNCM, L-NS-NCM, and S-NS-NCM at a current density of 300 mA·g^{-1}. The potential range was −0.85–0.55 V *vs.* Hg/HgO.
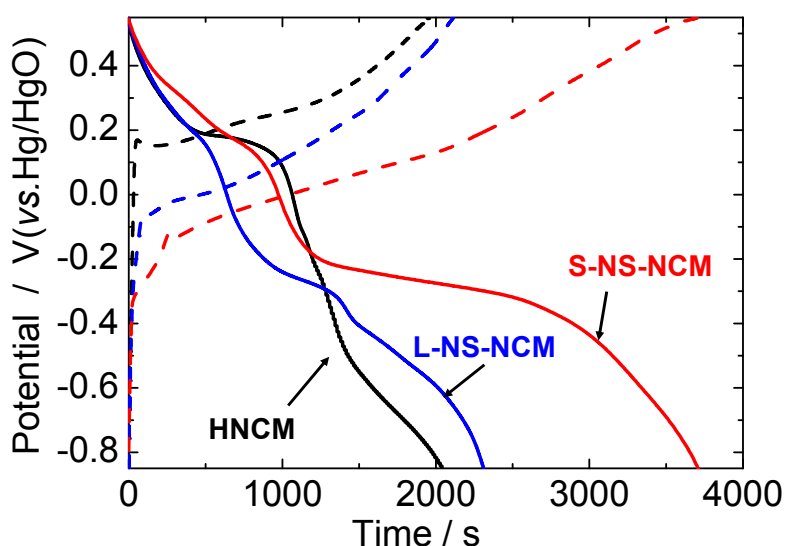
2.2.4. Cycle Capabilities

Figure 7 shows the cycle performances of HNCM, L-NS-NCM, and S-NS-NCM at a current density of 300 mA·g^{-1}. The cycle measurement for HNCM was conducted using the electrode after CV measurement. HNCM and L-NS-NCM exhibited good cycle stabilities and similar capacitances of 441 and 472 F·g^{-1}, respectively, in the first cycle, and maintained capacitances of 361 and 479 F·g^{-1} even in the 100th cycle. On the other hand, S-NS-NCM exhibited a large capacitance of 804 F·g^{-1} in the first cycle; however, the capacitance decreased rapidly during the first 50 cycles. The cycle performances of HNCM and L-NS-NCM for longer cycles were measured using new electrodes. Figure 8 shows the normalized cycle performances of HNCM and L-NS-NCM at a current density of 1000 mA·g^{-1}. HNCM exhibited a large capacitance of 307 F·g^{-1} in the first cycle; however, the capacitance decreased rapidly to approximately 200 F·g^{-1} during the first 10 cycles but this value was maintained. On the other hand, L-NS-NCM exhibited good cycle performance and a capacitance of 218 F·g^{-1} (87% of that in the first cycle) was maintained even in the 1000th cycle. The difference in the cycle performances of these two compounds probably resulted from the difference in their microstructures. The decay in the capacitances of HNCM and S-NS-NCM seemed to result from microstructural changes in their layered structure during charge/discharge cycles. The original

microstructures may have been damaged by lattice volume changes or configuration (rotation, slide) changes in nanosheets during charge/discharge cycles. These effects were remarkable in the case of S-NS-NCM. Such microstructural changes led to blocking of electric/ionic conduction or loss of surface area, resulting in increased reaction resistances. On the other hand, the microstructure of L-NS-NCM was seemingly preserved during charge/discharge cycles, probably because its strongly interconnected layered structure with numerous pores composed of large-NS reduced the physical stress on the particles during charge/discharge cycles. Thus, the excellent cycle stability of L-NS-NCM seemed to have resulted from its strongly interconnected layered structure composed of large-NS.

Figure 7. Cycle stabilities of HNCM, L-NS-NCM, and S-NS-NCM at a current density of 300 mA·g^{-1}. The potential range was −0.85–0.55 V *vs.* Hg/HgO.

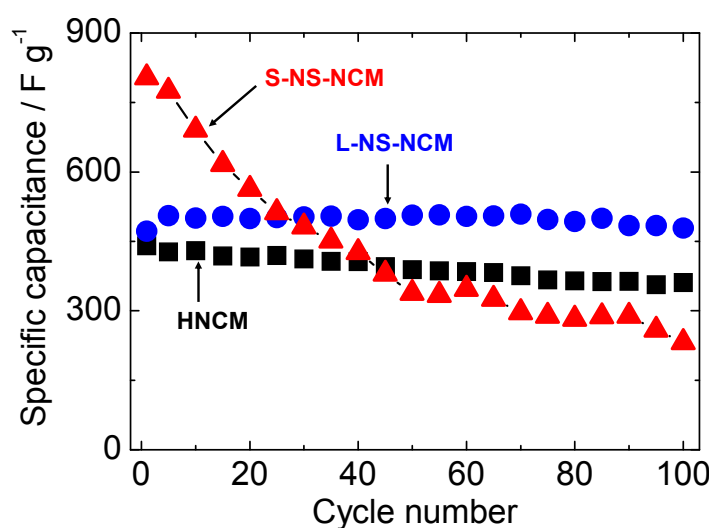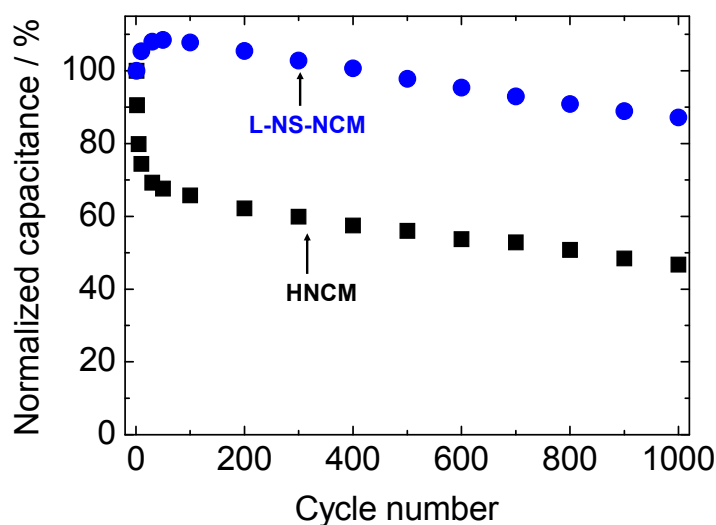**Figure 8.** Normalized cycle stabilities of HNCM and L-NS-NCM at a current density of 1000 mA g^{-1}. The potential range was −0.6–0.55 V *vs.* Hg/HgO.

2.2.5. Rate Capabilities

Figure 9 shows the rate capabilities of HNCM and S-NS-NCM. NS-NCM electrodes exhibited larger capacitances than HNCM did at all current densities. L-NS-NCM exhibited slightly larger capacitances than HNCM did in spite of its large particle size. S-NS-NCM exhibited a large capacitance of 1241 $F \cdot g^{-1}$ (395 $mAh \cdot g^{-1}$) at a current density of 50 $mA \cdot g^{-1}$, and 430 $F \cdot g^{-1}$ (100 $mAh \cdot g^{-1}$) at a large current density of 1000 $mA \cdot g^{-1}$. This large capacitance of 1241 $F \cdot g^{-1}$ corresponds to approximately 80% of the theoretical maximum capacitance of the redox reactions of Ni^{4+}/Ni^{2+}, Co^{3+}/Co^{2+}, and Mn^{4+}/Mn^{2+} (~1250 $F \cdot g^{-1}$, 400 $mAh \cdot g^{-1}$). This capacitance is larger than that reported for RuO_2/C composites (980 $F \cdot g^{-1}$) [8], and a capacitance larger than this has not been reported for powder (except for very thin films) electrode materials for electrochemical capacitors [4–22].

Figure 9. Rate capabilities of HNCM and S-NS-NCM. The potential range was −0.6–0.55 V *vs.* Hg/HgO.
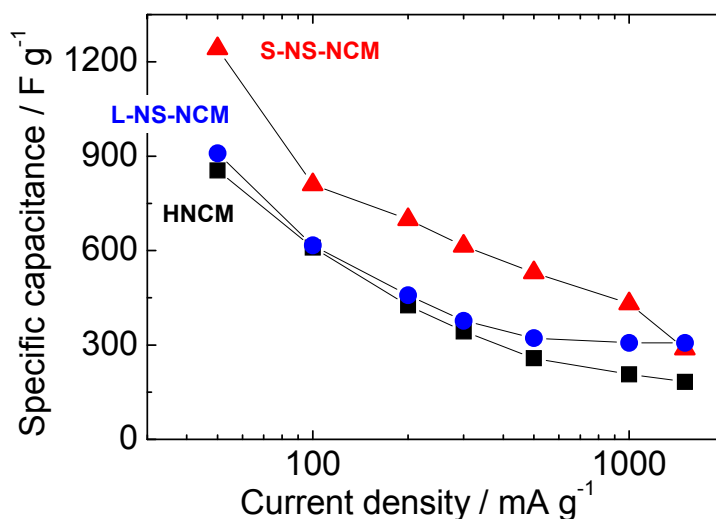
2.2.6. AC Impedance Measurements

AC impedance measurements were conducted in order to confirm the difference in the reaction resistances of these electrodes. Figures 10 and 11 show AC impedance plots for the electrodes in the first charge cycle and the equivalent circuit used for curve fitting, respectively. The reaction resistances obtained by curve fitting using an equivalent circuit are listed in Table 2. The real-axis intercept in the high-frequency region corresponds to the bulk resistance R_{bulk}, which includes the electronic resistance of the active material, contact resistance with the current collector, and electrolyte resistance. The curve in the high-to-medium frequency region corresponds to the charge-transfer reaction R_{ct}. In this region, an electron from the external circuit is inserted into MeO_2, and this is followed by the insertion reaction of a proton in order to maintain the charge balance. The straight-line sections with slopes of 45–90° in the low-frequency region correspond to ionic diffusion in the electrode [47,48].

S-NS-NCM had the largest double-layer capacitance; moreover, the double-layer capacitance of L-NS-NCM was slightly larger than that of HNCM. The double-layer capacitance increased with the specific surface area. The ionic diffusion resistance and charge-transfer resistance were the largest and

smallest for L-NS-NCM and S-NS-NCM, respectively. The differences in these resistances are also considered to have resulted from the difference in the microstructures of these electrodes, as discussed in the next section.

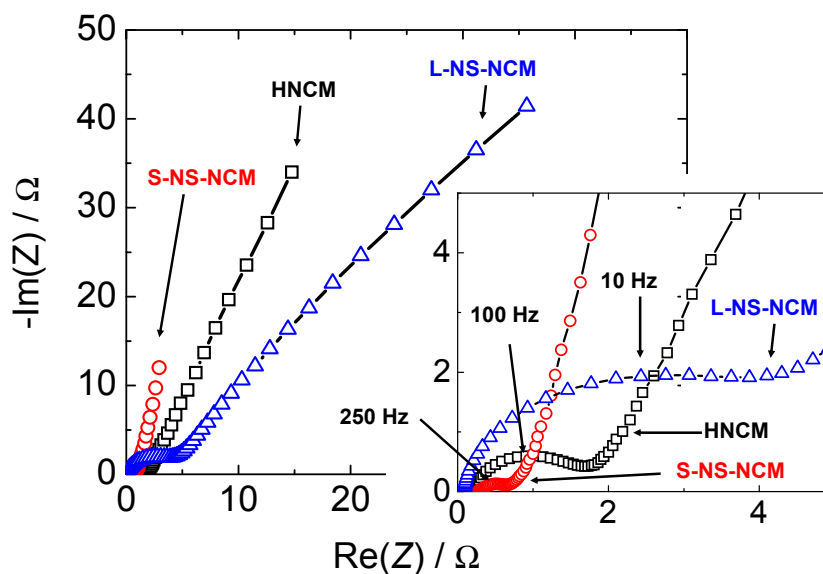**Figure 10.** AC-impedance plots for HNCM, L-NS-NCM, and S-NS-NCM.

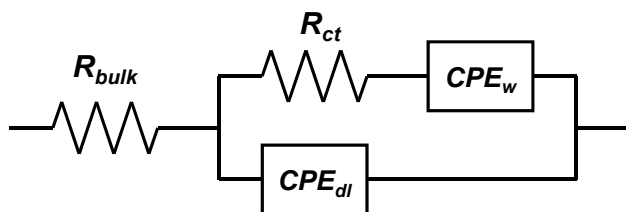**Figure 11.** Equivalent circuit used for curve fitting.

Table 2. Reaction resistances of HNCM, L-NS-NCM, and S-NS-NCM obtained by curve fitting with an equivalent circuit.

Electrodes	Charge transfer resistance (Ω)	Double-layer capacitance ($m^2\,g^{-1}$)	Diffusion resistance (qualitative)
HNCM	1.53	2.2×10^{-3}	Intermediate
L-NS-NCM	3.81	2.9×10^{-3}	Large
S-NS-NCM	0.56	5.7×10^{-2}	Small

2.2.7. Discussion

The ionic diffusion process in an electrode involves ionic diffusion in the solid state, as well as in the electrolyte-filled pores. The ionic diffusion resistance obtained from the AC impedance measurements also involves the contributions of these two diffusion processes. The ionic diffusion processes in the solid state and in the pores are largely influenced by particle size and pore volume. Since L-NS-NCM had a large particle size and a small pore volume, its ionic diffusion resistance was more than those of the other electrodes.

HNCM and S-NS-NCM had similar particle sizes but different microstructures. HNCM had a homogeneous layered structure with a small surface area and pore volume, while S-NS-NCM had a heterogeneous layered structure with a large surface area and pore volume. For layer-structured oxides, the diffusion rate of cations as alkaline metal ions is large in parallel and small perpendicular to the layers [49]. Therefore, in a material with a homogeneous layered structure consisting of regularly stacked layers, such as HNCM, a proton has to travel a long distance to reach the inner part of the active material. In contrast, proton diffusion should be smooth in S-NS-NCM through the electrolyte in the pores and inside the nanosheets with small lateral sizes; this could be the reason for the difference in the diffusion resistances of HNCM and S-NS-NCM.

A large surface area, fast transport of ions, and sufficient supply of electrons are important factors to achieve a fast charge-transfer reaction. When an electrode has a large pore volume, enough electronic conductivity, and large specific surface area, the charge-transfer resistance will be small. All the aforementioned conditions are assumed to be present in S-NS-NCM. It had a small charge-transfer resistance because of a heterogeneous layered structure with a large surface area and pore volume.

Accordingly, the large capacitance and high rate capability of S-NS-NCM as compared to the other electrodes can be attributed to the heterogeneous layered structure of S-NS-NCM with a large surface area and pore volume.

The capacitances of L-NS-NCM were larger than that of HNCM in most cases, although the reaction resistances in the 1st charge cycle were larger than those for HNCM. Original microstructures may have been lost or damaged by changes in the cell volume or sliding of the oxide layer during charge/discharge cycles, especially in S-NS-NCM because nanosheets seemed to be weakly interconnected in S-NS-NCM. This microstructural change may have caused physical damage of particles, loss of surface areas, or electric conductive passes, which resulted in increased reaction resistances. On the other hand, the microstructure of L-NS-NCM was seemingly preserved during charge/discharge cycles, probably because its strongly interconnected layered structure with numerous pores composed of large-NS reduced the physical stress on the particles during charge/discharge cycles. Thus, the excellent cycle stability of L-NS-NCM seemed to have resulted from the strongly interconnected layered structure composed of large-NS.

On the basis of these effects, the restacking of $(Ni_{1/3}Co_{1/3}Mn_{1/3})O_2$ nanosheets was found to be an effective method to improve the electrode properties of layer-structured materials for electrochemical capacitors with high rate capability, large specific capacitance, and good cycle stability. The electrode properties of HNCM could be further improved by precise microstructural control achieved through nanosheet restacking. Particles with an intermediate microstructure between those of S- and L-NS-NCM, for which strong interconnection of nanosheets and large surface area co-exist, will have high rate capability, large specific capacitance, and good cycle stability. The rate capability can be improved by fabricating homogeneous nanosheet composites and electronically conductive additives; moreover, the cycle stability can be enhanced by microstructural control such as interlayer modification through the use of different kinds of cations.

3. Experimental Section

3.1. Material Synthesis

Nanosheets were obtained by the exfoliation of layer-structured HNCM [41]. Layer-structured LNCM was synthesized via a co-precipitation method [28]. Aqueous solutions of $NiSO_4$, $CoSO_4$, and $MnSO_4$ (Ni:Co:Mn = 1:1:1) with a total concentration of 2.0 M were added into a continuously stirred reactor under an Ar atmosphere. Simultaneously, a 2.0 M NaOH aqueous solution as a pH conditioner and an NH_4OH aqueous solution (metal ion:NH_4OH = 1:1) as a chelating agent were also separately added into the reactor. The co-precipitated particles were stirred at 80 °C for 12 h. The pH value during co-precipitation was maintained at 12. The obtained $(Ni_{1/3}Co_{1/3}Mn_{1/3})(OH)_2$ particles were filtered, washed, and dried at 80 °C in vacuum for 2 h. The LiOH·H_2O powders were then mixed and calcined. The mixture was first heated at 480 °C for 5 h in air and was then calcined at 1000 °C for 10 h in air to obtain LNCM powders. To obtain HNCM, the interlayer Li was exchanged for protons by stirring LNCM in a 1 M HCl aqueous solution at room temperature for 5 days, during which time the HCl solution was refreshed daily. A colloidal suspension of $(Ni_{1/3}Co_{1/3}Mn_{1/3})O_2$ nanosheets was obtained by reacting HNCM with tetramethylammonium hydroxide at room temperature for 14 days. A colloidal suspension of small- and large-NS was obtained by multistep centrifugation at different rotation speeds, as reported previously [21]. As-prepared S-NS-NCM and L-NS-NCM were obtained by reacting the $(Ni_{1/3}Co_{1/3}Mn_{1/3})O_2$ nanosheet colloidal suspensions with a 1 M HCl aqueous solution. The particle size of as-prepared S-NS-NCM was reduced by ball milling in ethanol at 200 rpm for 1 h, after which the ethanol was evaporated.

3.2. Characterizations

The crystal structures of the samples were confirmed by performing XRD analysis using a D8 ADVANCE diffractometer (Bruker, Billerica, MA, USA). The morphologies of the delaminated nanosheets were observed by AFM performed using a SPS3100 microscope (Seiko Instruments, Chiba, Japan). The particle morphologies were observed by SEM performed using S-4500 and SU-8000 microscopes (Hitachi High-Technologies, Tokyo, Japan). The cross-section processing of the particle samples and the observation were performed by double beam system of the focused ion beam and the SEM (FIB-SEM) system, using XVision210DB (Hitachi High-Tech Science, Tokyo, Japan). The specific surface area and pore volume of the samples were determined by a gas absorption method carried out using a Micromeritics TriStar 3000 analyzer.

3.3. Electrochemical Measurements

HNCM and NS-NCM electrodes were prepared by mixing the active material (HNCM or NS-NCM), acetylene black, and PTFE in a weight ratio of 5:5:1, and pressing the mixture onto a Ti mesh under a loading of 5 mg·cm^{-2}. Electrochemical measurements were performed using a three-electrode cell with a Hg/HgO electrode as the reference electrode and a Pt mesh as the counter electrode. KOH aqueous solutions with a concentration of 1 M were used as the electrolyte. In addition, galvanostatic charge/discharge tests were carried out using a Solartron 1470E Cell-Test

system (Solartron Analytical, Hampshire, UK), a HZ-3000 system (Hokuto Denko, Tokyo, Japan), and a VMP3 (BioLogic, Grenoble, France). AC impedance measurements were carried out using the BioLogic VMP3.

4. Conclusions

The S-NS-NCM electrode composed of $(Ni_{1/3}Co_{1/3}Mn_{1/3})O_2$ nanosheets with a small lateral size of 50–100 nm exhibited very large capacitance of 1241 $F \cdot g^{-1}$ (395 $mAh \cdot g^{-1}$) at a current density of 50 $mA \cdot g^{-1}$, and 430 $F \cdot g^{-1}$ (100 $mAh \cdot g^{-1}$) at a large current density of 1000 $mA \cdot g^{-1}$ in a 1 M KOH aqueous solution. The heterogeneous layered structure of S-NS-NCM with a large surface area and pore volume contributed to an increase in the reaction surface area and smooth ion diffusion in the electrodes, resulting in a small reaction resistance. Electrodes of large nanosheets with sizes of 50–600 nm and surface areas slightly larger than that of HNCM exhibited good cycle stability, maintaining 218 $F \cdot g^{-1}$ (87% of that in the first cycle) at 1000 $mA \cdot g^{-1}$ even in the 1000th cycle. Microstructural control through the restacking of $(Ni_{1/3}Co_{1/3}Mn_{1/3})O_2$ nanosheets was found to be effective for improving the electrochemical properties of HNCM.

Acknowledgments

References

1. Nishino, A. Capacitors: Operating principles, current market and technical trends. *J. Power Sources* **1996**, *60*, 137–147.
2. Simon, P.; Gogotsi, Y. Materials for electrochemical capacitors. *Nat. Mater.* **2008**, *7*, 845–854.
3. Faggioli, E.; Rena, P.; Danel, V.; Andrieu, X.; Mallant, R.; Kahlen, H. Supercapacitors for the energy management of electric vehicles. *J. Power Sources* **1999**, *84*, 261–269.
4. Zheng, J.P.; Cygan, P.J.; Jow, T.R. Hydrous ruthenium oxide as an electrode material for electrochemical capacitors. *J. Electrochem. Soc.* **1995**, *142*, 2699–2703.
5. Naoi, K.; Ishimoto, S.; Ogihara, N.; Nakagawa, Y.; Hatta, S. Encapsulation of nanodot ruthenium oxide into KB for electrochemical capacitors. *J. Electrochem. Soc.* **2009**, *156*, A52–A59.
6. Sugimoto, W.; Yokoshima, K.; Ohuchi, K.; Murakami, Y.; Takasu, Y. Fabrication of thin-film, flexible, and transparent electrodes composed of ruthenic acid nanosheets by electrophoretic deposition and application to electrochemical capacitors. *J. Electrochem. Soc.* **2006**, *153*, A255–A260.
7. Hu, C.-C.; Chen, W.-C. Effects of substrates on the capacitive performance of $RuO_x \cdot nH_2O$ and activated carbon-RuO_x electrodes for supercapacitors. *Electrochim. Acta* **2004**, *49*, 3469–3477.

8. Chen, W.-C.; Hu, C.-C.; Wang, C.-C.; Min, C.-K. Electrochemical characterization of activated carbon-ruthenium oxide nanoparticles composites for supercapacitors. *J. Power Sources* **2004**, *125*, 292–298.

9. Yang, Y.; Kim, D.; Yang, M.; Schmuki, P. Vertically aligned mixed V_2O_5-TiO_2 nanotube arrays for supercapacitor applications. *Chem. Commun.* **2011**, *47*, 7746–7748.

10. Zheng, L.; Xu, Y.; Jin, D.; Xie, Y. Novel metastable hexagonal MoO_3 nanobelts: Synthesis, photochromic, and electrochromic properties. *Chem. Mater.* **2009**, *21*, 5681–5690.

11. Pang, S.C.; Anderson, M.A.; Chapman, T.W. Novel electrode materials for thin-film ultracapacitors: Comparison of electrochemical properties of sol-gel-derived and electrodeposited manganese dioxide. *J. Electrochem. Soc.* **2000**, *147*, 444–450.

12. Sivakkumar, S.R.; Ko, J.; Kim, D.; Kim, B.C.; Wallace, G.G. Performance evaluation of CNT/polypyrrole/MnO_2 composite electrodes for electrochemical capacitors. *Electrochim. Acta* **2007**, *52*, 7377–7385.

13. Toupin, M.; Brousse, T.; Belanger, D. Charge storage mechanism of MnO_2 electrode used in aqueous electrochemical capacitor. *Chem. Mater.* **2004**, *16*, 3184–3190.

14. Wei, W.; Cui, X.; Chen, W.; Ivey, D.G Manganese oxide-based materials as electrochemical supercapacitor electrodes. *Chem. Soc. Rev.* **2011**, *40*, 1697–1721.

15. Xu, C.-L.; Bao, S.-J.; Kong, L.-B.; Li, H.; Li, H.-L. Highly ordered MnO_2 nanowire array thin films on Ti/Si substrate as an electrode for electrochemical capacitor. *J. Solid State Chem.* **2006**, *179*, 1351–1355.

16. Jeong, Y.U.; Manthiram, A. Nanocrystalline manganese oxides for electrochemical capacitors with neutral electrolytes. *J. Electrochem. Soc.* **2002**, *149*, A1419–A1422.

17. Reddy, R.N.; Reddy, R.G. Sol-gel MnO_2 as an electrode material for electrochemical capacitors. *J. Power Sources* **2003**, *124*, 330–337.

18. Yuan, C.; Su, L.; Gao, B.; Zhang, X. Enhanced electrochemical stability and charge storage of MnO_2/carbon nanotubes composite modified by polyaniline coating layer in acidic electrolytes. *Electrochim. Acta* **2008**, *53*, 7039–7047.

19. Jang, H.; Suzuk, S.; Miyayama, M. Self-reassembled MnO_2 nanosheets for electrochemical capacitors in neutral aqueous solution. *J. Electrochem. Soc.* **2012**, 159, A1425–A1430.

20. Jang, H.; Suzuki, S.; Miyayama, M. Electrode properties of nanosheet-derived MnO_2 for electrochemical capacitors. *ECS Trans.* **2011**, *33*, 145–154.

21. Yano, M.; Suzuki, S.; Miyayama, M. MnO_2 nanosheets thin-film electrodes for electrochemical capacitors. *ECS Trans.* **2011**, *35*, 187–194.

22. Kintsu, Y.; Suzuki, S.; Miyayama, M. Electrochemical properties of $Ba(MnPO_4)_2 \cdot H_2O$ in alkaline aqueous electrolytes. *Ceramic Int.* **2013**, in press.

23. Xionghan, F.; Wenfeng, T.; Fan, L.; Qiaoyun, H.; Xiangwen, L. Pathways of birnessite formation in alkali medium. *Sci. China Ser. D* **2005**, *48*, 1438–1451.

24. Hem, J.D. Redox processes at surfaces of manganese oxide and their effects on aqueous metal ions. *Chem. Geol.* **1979**, *21*, 199–218.

25. McBreen, J. The electrochemistry of β-MnO_2 and γ-MnO_2 in alkaline electrolyte. *Electrochim. Acta* **1975**, *20*, 221–225.

26. Kang, S.-H.; Kim, J.; Stoll, M.E.; Abraham, D.; Amine, K. Layered Li(Ni$_{0.5-x}$Mn$_{0.5-x}$M$_{2x}'$)O$_2$ (M$'$=Co, Al, Ti; x = 0, 0.025) cathode materials for Li-ion rechargeable batteries. *J. Power Sources* **2002**, *112*, 41–48.

27. Ngala, J.K.; Chernova, N.A.; Ma, M.; Mamak, M.; Zavalij, P.Y.; Whittingham, M.S. The synthesis, characterization and electrochemical behavior of the layered LiNi$_{0.4}$Mn$_{0.4}$Co$_{0.2}$O$_2$ compound. *J. Mater. Chem.* **2004**, *14*, 214–220.

28. Lee, M.-H.; Kang, Y.-J.; Myung, S.-T.; Sung, Y.-K. Synthetic optimization of Li[Ni$_{1/3}$Co$_{1/3}$Mn$_{1/3}$]O$_2$ via co-precipitation. *Electrochim. Acta* **2004**, *50*, 939–948.

29. Park, S.H.; Yoon, C.S.; Kang, S.G.; Kim, H.-S.; Moon, S.-I.; Sun, Y.-K. Synthesis and structural characterization of layered Li[Ni$_{1/3}$Co$_{1/3}$Mn$_{1/3}$]O$_2$ cathode materials by ultrasonic spray pyrolysis method. *Electrochim. Acta* **2004**, *49*, 557–563.

30. Idemoto, Y.; Matsui, T. Thermodynamic stability, crystal structure, and cathodic performance of Li$_x$(Ni$_{1/3}$Co$_{1/3}$Mn$_{1/3}$)O$_2$ dependent on the synthetic process and Li content. *Solid State Ionics* **2008**, *179*, 625–635.

31. Shaju, K.M.; Subba Rao, G.V.; Chowdari, B.V.R. Performance of layered Li(Ni$_{1/3}$Co$_{1/3}$Mn$_{1/3}$)O$_2$ as cathode for Li-ion batteries. *Electrochim. Acta* **2002**, *48*, 145–151.

32. Koyama, Y.; Tanaka, I.; Adachi, H.; Makimura, Y.; Ohzuku, T. Crystal and electronic structures of superstructural Li$_{1-x}$[Ni$_{1/3}$Co$_{1/3}$Mn$_{1/3}$]O$_2$ (0 ≤ x ≤ 1). *J. Power Sources* **2003**, *119–121*, 644–648.

33. Kim, J.-M.; Chung, H.-T. The first cycle characteristics of Li[Ni$_{1/3}$Co$_{1/3}$Mn$_{1/3}$]O$_2$ charged up to 4.7 V. *Electrochim. Acta* **2004**, *49*, 937–944.

34. Liu, J.; Qiu, W.; Yu, L.; Zhao, H.; Li, T. Synthesis and electrochemical characterization of layered Li(Ni$_{1/3}$Co$_{1/3}$Mn$_{1/3}$)O$_2$ cathode materials by low-temperature solid-state reaction. *J. Alloys Compd.* **2008**, *449*, 326–330.

35. Yano, M.; Suzuki, S.; Miyayama, M.; Ohgaki, M. Electrochemical properties of layer-structured H$_x$(Ni$_{1/3}$Co$_{1/3}$Mn$_{1/3}$)O$_2$ for electrochemical capacitors in alkaline aqueous solutions. *J. Asian Ceram. Soc.* **2013**, submitted for publication.

36. Suzuki, S.; Takahashi, S.; Sato, K.; Miyayama, M. High-rate electrode properties of Li-Mn-oxide synthesized by reassembly of MnO$_2$ nanosheets for Li-ion battery. *Key Eng. Mater.* **2006**, *320*, 223–226.

37. Suzuki, S.; Miyayama, M. Lithium intercalation properties of reassembled titanate/carbon composites. *J. Electrochem. Soc.* **2007**, *154*, A438–A443.

38. Omomo, Y.; Sasaki, T.; Wang, L.; Watanabe, M. Redoxable nanosheet crystallites of MnO$_2$ derived via delamination of layered manganese oxide. *J. Am. Chem. Soc.* **2003**, *125*, 3568–3575.

39. Sakai, N.; Ebina, Y.; Takada, K.; Sasaki, T. Electronic band structure of titania semiconductor nanosheets revealed by electrochemical and photoelectrochemical studies. *J. Am. Chem. Soc.* **2004**, *126*, 5851–5858.

40. Liu, Z.-H.; Ooi, K.; Kanoh, H.; Tang, W.P.; Tomida, T. Swelling and delamination behaviors of birnessite-type manganese oxide by intercalation of tetraalkylammonium ions. *Langmuir* **2000**, *16*, 4154–4164.

41. Oh, E.-J.; Kim, T.W.; Lee, K.M.; Song, M.-S.; Jee, A.-Y.; Lim, S.T.; Ha, H.-W.; Lee, M.; Choy, J.-H.; Hwang, S.-J. Unilamellar nanosheet of layered manganese cobalt nickel oxide and its heterolayered film with polycations. *ACS Nano* **2010**, *4*, 4437–4444.

42. Benhaddad, L.; Makhloufi, L.; Messaoudi, B.; Takenouti, H. Reactivity of nanostructured MnO_2 in alkaline medium studied with a micro-cavity electrode: Effect of synthesizing temperature. *Appl. Mater. Interfaces* **2009**, *1*, 424–432.

43. Kozawa, A.; Yeager, J.F. The cathodic reduction mechanism of electrolytic manganese dioxide in alkaline electrolyte. *J. Electrochem. Soc.* **1965**, *112*, 959–963.

44. Kozawa, A.; Yeager, J.F. Cathodic reduction mechanism of MnOOH to $Mn(OH)_2$ in alkaline electyrolyte. *J. Electrochem. Soc.* **1968**, *115*, 1003–1007.

45. Zhang, Y.; Zhou, Z.; Yan, J. Electrochemical behaviour of $Ni(OH)_2$ ultrafine powder. *J. Power Sources* **1998**, *75*, 283–287.

46. Gupta, V.; Kusahara, T.; Toyoma, H.; Gupta, S.; Miura, N. Potentiostatically deposited nanostructured α-$Co(OH)_2$: A high performance electrode material for redox capacitors. *Electrochem. Commun.* **2007**, *9*, 2315–2319.

47. Atlung, S.; Jacobsen, T. On the *ac*-impedance of electroactive powders. γ-manganese dioxide. *Electrochim. Acta* **1976**, *21*, 575–584.

48. Qu, D. Application of a.c. impedance technique to the study of the proton diffusion process in the porous MnO_2 electrode. *Electrochim. Acta* **2003**, *48*, 1675–1684.

49. Sakamoto, K.; Hirayama, M.; Konishi, H.; Sonoyama, N.; Dupre, N.; Guyomard, D.; Tamura, K.; Mizuki, J.; Kanno, R. Structural changes in surface and bulk $LiNi_{0.5}Mn_{0.5}O_2$ during electrochemical reaction on epitaxial thin-film electrodes characterized by *in situ* X-ray scattering. *Phys. Chem. Chem. Phys.* **2010**, *12*, 3815–3823.